

Investigation of the point spread function of SAS and CSAS imaging using bandpass signals

Chencheng Ye^{1,2}, Ziliang Qiao², Hong Liang¹, Dieter Kraus²

¹ Northwestern Polytechnical University, 710072 Xi'an China, E-Mail: cye001@stud.hs-bremen.de

² City University of Applied Sciences, 28199 Bremen, E-Mail: dieter.kraus@hs-bremen.de

Introduction

In the past decades, considerable attention has been paid to the application of ultrasonic reflection tomography in various fields such as medical imaging [1]-[2] and structure monitoring [3]. Among them, synthetic aperture techniques [4]-[5] have attracted extensive interest because of superior resolution performance. However, since the positions of the scatterers of a target typically do not exactly coincide with the pixel centers of the sonar image, residual phase errors may remain after phase compensation which can affect the imaging performance. Therefore, the sensitivity of the point spread function (PSF) with regard to the displacement of a point scatterer from the pixel center is investigated for a synthetic aperture sonar (SAS) and a circular synthetic aperture sonar (CSAS) in this paper. First, the typical processing steps for bandpass signals in imaging sonar systems as well as SAS and CSAS imaging methods using back-projection are described mathematically. Then the effect of the residual phase errors on the PSF of a SAS and a CSAS using bandpass signals are compared. In the following sections, closed form expressions are derived for the calculation of the PSF, since they are more suitable for a comprehensive investigation due to the advantage of a lower computing load compared to simulation results. Finally, conclusions are drawn and recommendations for future work are presented.

Synthetic Aperture Fundamentals

Synthetic Aperture Bandpass Model

Given an extended object within the 2-dimensional interval

$$S = [X_t - X_0, X_t + X_0] \times [Y_t - Y_0, Y_t + Y_0]$$

in the imaging scene, the reflectivity at a particular point $q = (x, y)$ within S is denoted by $f(x, y)$, which is assumed to be independent of frequency and incidence angle of the impinging wave in order to simplify the model.

In a basic configuration of SAS or CSAS the transceiver emits the transmit signal repeatedly at time instants t_p from its current position as it travels along a line or a circle with constant speed respectively, where $p = 1, 2, \dots, M_p$ is the ping index of transmission time t_p . Simultaneously, the echoes reflected by the various scatterers in the scene are received superimposed by the transceiver at the same position under the stop-and-hop assumption [6].

Now, let

$$\tilde{s}_T^{\text{BP}}(t) = \text{Re}\{s_{T,+}^{\text{BP}}(t)\} = \text{Re}\{s_T^{\text{LP}}(t)e^{j\omega_c t}\} \quad (1)$$

denote the transmitted real bandpass signal, where $s_{T,+}^{\text{BP}}(t)$, $s_T^{\text{LP}}(t)$ and ω_c correspond to the analytical signal and

complex envelope of the transmitted signal as well as the carrier frequency. Accordingly, the real bandpass signal received at ping p can be expressed as

$$\tilde{s}_R^{\text{BP}}(t|p) = \text{Re}\{s_{R,+}^{\text{BP}}(t|p)\} = \text{Re}\{s_R^{\text{LP}}(t|p)e^{j\omega_c t}\}, \quad (2)$$

where $s_{R,+}^{\text{BP}}(t|p)$ and $s_R^{\text{LP}}(t|p)$ denote the corresponding analytical signal and complex envelope. Due to the measurement procedure mentioned above the analytical signal $s_{R,+}^{\text{BP}}(t|p)$ can be expressed as an integral of individually weighted and delayed versions of the transmitted signal as follows

$$s_{R,+}^{\text{BP}}(t|p) = \int_{X_t-X_0}^{X_t+X_0} \int_{Y_t-Y_0}^{Y_t+Y_0} f(x, y) B(\theta(x, y|p)) \times s_{T,+}^{\text{BP}}(t - \tau(x, y|p)) dx dy + v_+^{\text{BP}}(t|p) \quad (3)$$

$$\text{with } p = 0, 1, \dots, M_p - 1, t \in [0, 2R_{\max}/c + T],$$

where $B(\theta)$ denotes the beam pattern of the transceiver, T is the pulse length of the transmitted signal and c the sound speed. Moreover, depending on the transceiver position in the p -th ping, $\theta(x, y|p)$ and $\tau(x, y|p)$ define the angle and round-trip travel time as function of $(x, y) \in S$. Finally, $v_+^{\text{BP}}(t|p)$ represents analytical signal of real bandpass noise.

Next, the received bandpass signal is quadrature demodulated (QD) to gain the according lowpass signal

$$s_R^{\text{LP}}(t|p) = s_{R,+}^{\text{BP}}(t|p)e^{-j\omega_c t} = \int_{X_t-X_0}^{X_t+X_0} \int_{Y_t-Y_0}^{Y_t+Y_0} f(x, y) B(\theta(x, y|p)) \times s_T^{\text{LP}}(t - \tau(x, y|p)) e^{-j\omega_c \tau(x, y|p)} dx dy + v^{\text{LP}}(t|p). \quad (4)$$

Finally, in order to maximize SNR and resolution, pulse compression is performed using matched filtering, the impulse response of which is the conjugate time-reversed transmitted signal. Hence, the pulse compressed signal is determined by

$$s_R^{\text{MF}}(t|p) = \int_{-\infty}^{\infty} s_R^{\text{LP}}(u|p) h_{\text{MF}}(t-u) du = \int_{-\infty}^{\infty} s_R^{\text{LP}}(u|p) (s_R^{\text{LP}}(u-t))^* du \quad (5)$$

In the absence of noise, inserting (4) into (5) leads to

$$s_R^{\text{MF}}(t|p) = \int_{X_t-X_0}^{X_t+X_0} \int_{Y_t-Y_0}^{Y_t+Y_0} f(x, y) B(\theta(x, y|p)) e^{-j\omega_c \tau(x, y|p)} \times \int_{-\infty}^{\infty} s_T^{\text{LP}}(u - \tau(x, y|p)) (s_T^{\text{LP}}(u-t))^* du dx dy = \int_{X_t-X_0}^{X_t+X_0} \int_{Y_t-Y_0}^{Y_t+Y_0} f(x, y) B(\theta(x, y|p)) e^{-j\omega_c \tau(x, y|p)} \times R_{s_T^{\text{LP}} s_T^{\text{LP}}}^*(t - \tau(x, y|p)) dx dy, \quad (6)$$

where $R_{s_T^{\text{LP}} s_T^{\text{LP}}}^*(t)$ denotes the autocorrelation function of transmitted signal.

Imaging methods for Bandpass Signals via Back-Projection in SAS and CSAS Mode

The imaging scene is divided into $M_x \times M_y$ pixels, where M_x and M_y represent the number of pixels along the positive x -axis and positive y -axis, respectively. Using vector notation, $\mathbf{g}_{kl} = (x_k, y_l)^T$ denotes the position vector of the k, l -th pixel center with $k = 1, 2, \dots, M_x$ and $l = 1, 2, \dots, M_y$. The size of a pixel is $\Delta x \times \Delta y$. The image is generated using the back-projection algorithm, where the value assigned to each pixel is obtained by accumulating the corresponding sample values of the $p = 1, 2, \dots, M_p$ pulse compressed echo signals in both SAS and CSAS mode. However, due to the different motion trajectories of SAS and CSAS, their formulae for estimating the reflectivity of the image scene via back-projection are derived separately.

SAS-Mode

Assuming the transceiver of beam-width $2\theta_{\text{phy}}$ moves along the x -axis, a point of the scene with the position vector \mathbf{g}_{kl} will be satisfactorily illuminated only if the x -coordinate of the transceiver location is within $(x_k - y_l \tan \theta_{\text{phy}}, x_k + y_l \tan \theta_{\text{phy}})$. Furthermore, the ping numbers, which correspond to the entry and exit of the interval, are designated by $p = p_0$ and $p = p_1$, respectively. Therefore, the estimate of the scene reflectivity function $f(x_k, y_l)$ using coherent back-projection can be determined by summation of the suitably delayed and phase-corrected pulse-compressed received signals of the pings $p = p_0, \dots, p_1$ as follows

$$\hat{f}(x_k, y_l) = \sum_{p=p_0}^{p_1} s_R^{\text{MF}}(\tau(\mathbf{g}_{kl}|p)|p) e^{j\omega_c \tau(\mathbf{g}_{kl}|p)}. \quad (7)$$

Supposing there is only one point target at $\mathbf{g}_t = (x_t, y_t)^T$ in the scene, i.e. $f(x, y) = f(x_t, y_t) \delta(x - x_t, y - y_t)$ with $\delta(\cdot, \cdot)$ denoting the 2-dimensional Dirac delta function, then inserting (6) in (7) the PSF of the SAS mode can be expressed by

$$\begin{aligned} \hat{f}(x_k, y_l) = & \sum_{p=p_0}^{p_1} f(x_t, y_t) R_{s_t^{\text{LP}} s_t^{\text{LP}}}(\tau(\mathbf{g}_{kl}|p) - \tau(\mathbf{g}_t|p)) \\ & \times B(\theta(\mathbf{g}_t|p)) e^{j\omega_c(\tau(\mathbf{g}_{kl}|p) - \tau(\mathbf{g}_t|p))} \end{aligned} \quad (8)$$

CSAS-Mode

Assuming the transceiver beam-width is large enough to ensure that all pixels in the imaging scene are illuminated by the transceiver for all M_p pings, the reflectivity of the scene at pixel center \mathbf{g}_{kl} can be estimated accordingly to (7) by coherent summation of M_p samples taken from the M_p pulse-compressed echo signals as follows

$$\hat{f}(x_k, y_l) = \sum_{p=1}^{M_p} s_R^{\text{MF}}(\tau(\mathbf{g}_{kl}|p)|p) e^{j\omega_c \tau(\mathbf{g}_{kl}|p)}. \quad (9)$$

Analogous to (8), the PSF of the CSAS mode can be represented by

$$\begin{aligned} \hat{f}(x_k, y_l) = & \sum_{p=1}^{M_p} f(x_t, y_t) R_{s_t^{\text{LP}} s_t^{\text{LP}}}(\tau(\mathbf{g}_{kl}|p) - \tau(\mathbf{g}_t|p)) \\ & \times B(\theta(\mathbf{g}_t|p)) e^{j\omega_c(\tau(\mathbf{g}_{kl}|p) - \tau(\mathbf{g}_t|p))} \end{aligned} \quad (10)$$

The main difference of the reconstruction formulae for the two modes consists in the number of pings used for the coherent processing.

Analysis of the Impact of Residual Phase Errors on the Point Spread Function

In practice, the locations of the scatterers of a target do not coincide with the pixel centers of an image. The displacements between scatterer locations and pixel centers cause residual phase errors, which affect the image quality differently in SAS and CSAS mode. Hence, the residual phase errors caused by a point target displaced in x and y direction by $\Delta x/2$ and $\Delta y/2$ from a pixel center are studied in this section.

In SAS mode, the residual phase error can be described by

$$\begin{aligned} \phi(\mathbf{g}_{kl}|p) = & \omega_c (\tau(\mathbf{g}_{kl}|p) - \tau(x_k + \Delta x/2, y_l + \Delta y/2|p)) \\ = & \omega_c \frac{2}{c} \left(y_l \sqrt{1 + \left(\frac{x_p - x_k}{y_l} \right)^2} - \left(y_l + \frac{\Delta y}{2} \right) \right. \\ & \times \left. \sqrt{1 + \left(\frac{x_p - x_k}{y_l + \Delta y/2} \right)^2} - \frac{(x_p - x_k)\Delta x}{(y_l + \Delta y/2)^2} + \frac{(\Delta x/2)^2}{(y_l + \Delta y/2)^2} \right) \end{aligned} \quad (11)$$

Applying $\sqrt{1+x} \approx 1+x/2$ for $|x| \ll 1$, ignoring the quadratic term in Δx and exploiting $y_l \approx y_l + \Delta y/2$ one can derive

$$\phi(\mathbf{g}_{kl}|p) \approx \omega_c \frac{2}{c} \left(\frac{x_p - x_k}{y_l} \frac{\Delta x}{2} - \frac{\Delta y}{2} \right) \quad (12)$$

In case that the x -coordinate of the transceiver position and the pixel center coincide, i.e. $x_p = x_k$ (center of the synthetic aperture), the residual phase error becomes

$$\phi_{\text{center}} = -\frac{\omega_c \Delta y}{c} \quad (13)$$

For $x_p = x_k - y_l \tan \theta_{\text{phy}}$ (start of the synthetic aperture) and $x_p = x_k + y_l \tan \theta_{\text{phy}}$ (end of the synthetic aperture) as well as assuming $\tan \theta_{\text{phy}} \approx \theta_{\text{phy}}$ (valid in practice) the residual phase errors can be approximately determined by

$$\phi_{\text{start}} \approx -\frac{\omega_c}{c} (\theta_{\text{phy}} \Delta x + \Delta y) \quad (14)$$

and

$$\phi_{\text{end}} \approx \frac{\omega_c}{c} (\theta_{\text{phy}} \Delta x - \Delta y), \quad (15)$$

respectively. Therefore, the difference in the residual phase error between the start respectively end position and the center position can be calculated by

$$\Delta\phi = \mp \frac{\omega_c}{c} \theta_{\text{phy}} \Delta x, \quad |\Delta\phi| \leq \frac{2\pi f_c}{c} \frac{1}{2} \frac{c}{f_c D_{\text{phy}}} \frac{D_{\text{phy}}}{2} = \frac{\pi}{2} \quad (16)$$

assuming $\Delta x \leq D_{\text{phy}}/2$ to be not greater than the along track SAS resolution with D_{phy} denoting the along track aperture of the transceiver. Thus, the residual phase error satisfies $-\pi/2 \leq \Delta\phi \leq \pi/2$, where the interval limits are independent from the center frequency f_c and the along track aperture D_{phy} of the transceiver.

In the following, the residual phase error for the CSAS mode is derived and analyzed. Since the transceiver follows a circular path, polar coordinates are more suitable than Cartesian coordinates to investigate the residual phase error. The polar coordinates of the pixel centers and the displaced point target are given by

$$\tilde{\mathbf{g}}_{kl} = (r_{kl}, \theta_{kl})^T = \left(\sqrt{x_k^2 + y_l^2}, \tan^{-1}(y_l/x_k) \right)^T, \quad (17)$$

and $\tilde{\mathbf{g}}_t = (r_t, \theta_t)^T$ with

$$\begin{aligned} r_t &= \sqrt{(x_k + \Delta x/2)^2 + (y_l + \Delta y/2)^2}, \\ \theta_t &= \tan^{-1}((y_l + \Delta y/2)/(x_k + \Delta x/2)). \end{aligned} \quad (18)$$

respectively. Denoting the position of the transceiver at ping p in polar coordinates as $\tilde{\mathbf{g}}_p = (r_p, \theta_p)^T$, the residual phase error is formulated as

$$\begin{aligned} \phi(\tilde{\mathbf{g}}_{kl}|p) &= \omega_c (\tilde{\tau}(\tilde{\mathbf{g}}_{kl}|p) - \tilde{\tau}(\tilde{\mathbf{g}}_t|p)) \\ &= \omega_c \frac{2r_p}{c} \left(\sqrt{1 + (r_{kl}/r_p)^2 - 2r_{kl}\cos(\theta_p - \theta_{kl})/r_p} \right. \\ &\quad \left. - \sqrt{1 + (r_t/r_p)^2 - 2r_{kl}\cos(\theta_p - \theta_t)/r_p} \right). \end{aligned} \quad (19)$$

Assuming that the point target and pixel center are close to the center of the circle, i.e. $r_t \ll r_p$ and $r_{kl} \ll r_p$, and applying $\sqrt{1+x} \approx 1+x/2$ as well as $\cos(\alpha-\beta) = \cos\alpha\cos\beta + \sin\alpha\sin\beta$, $\phi(\tilde{\mathbf{g}}_{kl}|p)$ can be approximated by

$$\begin{aligned} \phi(\tilde{\mathbf{g}}_{kl}|p) &\approx 2\frac{\omega_c}{c} (r_t \cos(\theta_p - \theta_t) - r_{kl} \cos(\theta_p - \theta_{kl})) \\ &\approx \frac{\omega_c}{c} \frac{1}{r_p} (x_p \Delta x + y_p \Delta y) = \frac{\omega_c}{c} r_\Delta \cos(\theta_p - \theta_\Delta) \end{aligned} \quad (20)$$

with $r_\Delta = \sqrt{(\Delta x)^2 + (\Delta y)^2}$ and $\theta_\Delta = \tan^{-1}(\Delta y/\Delta x)$. Hence, the residual phase error satisfies

$$\phi_{\min} = -\frac{\omega_c}{c} r_\Delta \leq \phi(\tilde{\mathbf{g}}_{kl}|p) \leq \frac{\omega_c}{c} r_\Delta = \phi_{\max}, \quad (21)$$

where the interval limits are taken for $\theta_p = \theta_\Delta + \pi$ and $\theta_p = \theta_\Delta$, respectively, i.e. if $\mathbf{g}_p \parallel (\Delta x, \Delta y)^T$. The residual phase error becomes zero if $\mathbf{g}_p \perp (\Delta x, \Delta y)^T$ holds. In summary, it can be concluded from (21) that the range of variation of the residual phase error in the CSAS mode is proportional to the center frequency and pixel size and has no upper limit. It should also be noted that the imaging quality can be severely impaired due to the destructive superposition of the pulse-compressed echo signals for $\phi_{\max} - \phi_{\min} \geq \pi$.

Experimental Investigations

Results on the residual phase error

In the previous section, the analytical results for the residual phase error were derived regardless of a specific bandpass signal and transceiver geometry. For the subsequent experimental investigations, the signal bandwidth is set to $B = 40$ kHz and the point target is displaced by $(\Delta x/2, \Delta y/2)^T$ from the pixel center $(0, y)^T$ with the pixel size given by

$$\Delta x = D_{\text{phy}}/2 \text{ and } \Delta y = c/(2B)$$

for the SAS mode and from the pixel center $(0,0)^T$ with the pixel size given by

$$\Delta x = \Delta y = c/(2B)$$

for the CSAS mode.

Figure 1 shows the absolute and relative residual phase errors of the pulse-compressed echo signals received by the transceiver at $(x_p, y_p)^T = (\alpha y \tan \theta_{\text{phy}}, 0)^T$, $\alpha = -1, -0.5, 0, 0.5, 1$ for

the two center frequencies $f_c = 300$ kHz and $f_c = 500$ kHz. In Figure 1, relative residual phase errors remain in the range from 0° to 90° for different center frequencies while absolute residual phase errors change according to center frequency.

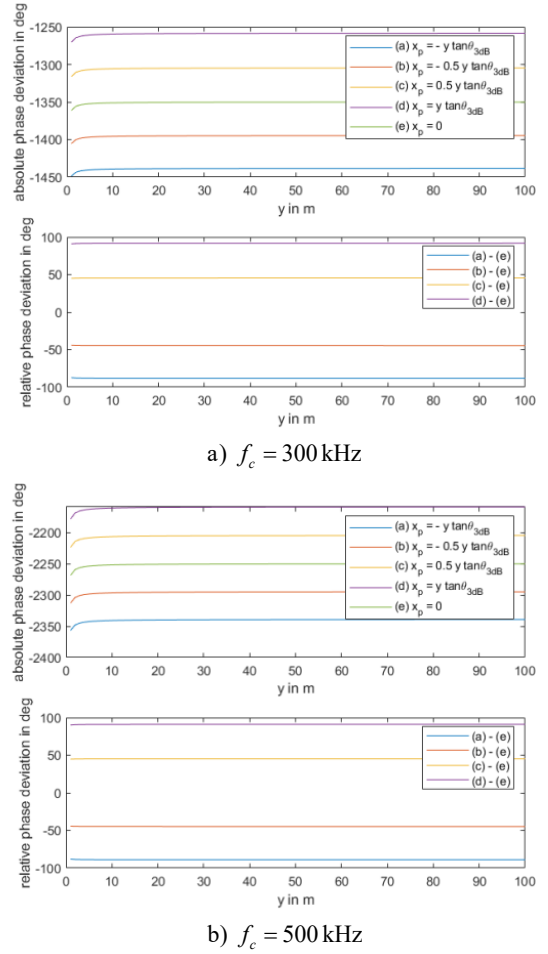


Figure 1: Analytical results of residual phase errors in SAS mode.

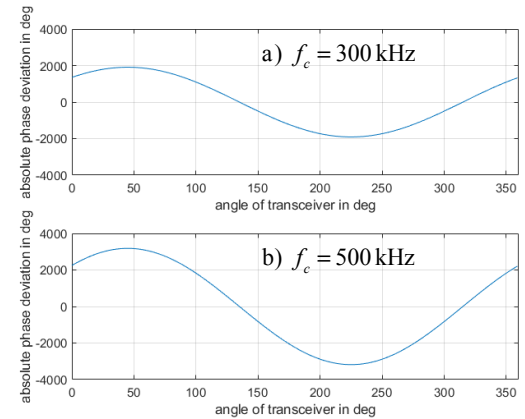


Figure 2: Analytical results of residual phase errors in CSAS mode.

Absolute residual phase errors of pulse-compressed echoes received by the transceiver moving over the circle from 0° to 360° in CSAS mode are depicted in Figure 2. It can be observed that the maximum and minimum residual phase errors are obtained at 45° and 225° , and the observation agrees with our previous analysis. In addition, both the absolute and the relative residual phase errors increase with increasing center frequency.

Results on the PSF

LFM signal is chosen as the typical bandpass waveform to verify the effect of the residual phase error on the PSF. However, instead of simulating all steps from transmitting the signal over several intermediate steps up to the back-projection algorithm, the PSF can be calculated in rather closed form after inserting the autocorrelation function of the LFM signals into (8) and (10), which is more suitable for experimental investigations due to a significantly lower computing load. With increasing sampling frequency, the simulation results approximate the results of the closed form.

In SAS and CSAS mode the same LFM signal is used with $f_c = 300$ kHz, $B = 40$ kHz, $T = 10$ ms and $K = B/T = 4$ MHz/s. The transducer size is assumed to be $d = 0.05$ m in SAS mode. Assuming $c = 1500$ m/s the beam width is $2\theta_{\text{phy}} = c/(f_c d) = 0.1$ (radians). As a result, the along-track and range resolution are 2.5 cm and 1.875 cm, respectively and the pixel size is set to $10 \text{ mm} \times 10 \text{ mm}$. The imaging scene given by $[20 \text{ m}, 24 \text{ m}] \times [20 \text{ m}, 24 \text{ m}] \subset \mathbb{R}^2$ is divided into 401×401 pixels. The range cut of the PSF through the peak value is plotted in Figure 3a) when the point target is located in (22 m, 22 m), which agrees with a particular pixel center in the imaging scene. Its counterpart is depicted in Figure 3b) when the point target has a displacement of 5 mm in both the x- and y-axis from the pixel center.

For CSAS, the image scene is set to the area $[-1 \text{ m}, 1 \text{ m}] \times [-1 \text{ m}, 1 \text{ m}] \subset \mathbb{R}^2$ and the radius of the circle with the center in the origin is assumed to be 20 m. Due to the range resolution of 1.875 cm, the pixel size is set to $10 \text{ mm} \times 10 \text{ mm}$ again and the imaging scene is divided into 201×201 pixels. Figure 4a) presents the range cut of the PSF through the peak value when the point target is in the origin while the corresponding results of the displaced point target located in (5 mm, 5 mm) are shown in Figure 4b).

Closer inspection of Figure 3 shows the corresponding peak values are 2.21 and 1.83 for the point target with and without displacement, which verifies the conclusion that residual phase errors have little impact on the PSF in SAS mode. However, the peak value drops sharply from 3.6 to 0.17 for the point target with displacement in CSAS mode, which is shown in Figure 4. The significant change results from the destructive interference caused by the residual phase errors.

Summary and Outlook

This paper examines the effects of residual phase errors on the PSF and thus on the imaging performance of SAS and CSAS systems when bandpass signals are used. In both cases, echo signals are coherently superimposed over certain synthetic aperture lengths to estimate the reflectivity at a particular pixel. For SAS, the synthetic aperture length adjusts automatically according to pixel range position and carrier frequency, thus the relative residual phase errors remain within a small range, which is acceptable for coherent superposition. In comparison with that, both absolute and relative residual phase errors increase with carrier frequency and pixel size for CSAS without upper limit, which consequently may lead to a destructive superposition of the echo signals. To verify the conclusions, numerical results are presented using the

closed form expressions derived for the residual phase errors and the PSF. In order to take advantage of the higher resolution through coherent processing, future work in CSAS mode should be aimed at finding solutions to reduce the residual phase errors caused by the displacement between the target scatterers and the pixel centers.

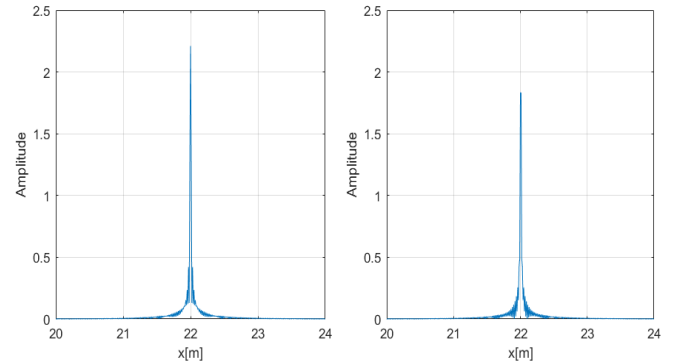


Figure 3: PSF image cut in SAS mode for target at
a) (22m, 22m), b) (21.995m, 21.995m)

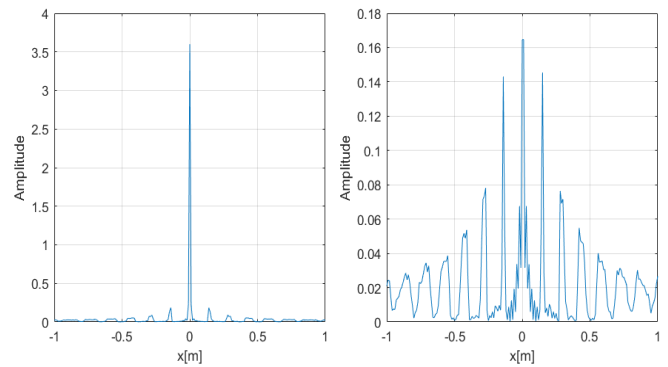


Figure 4: PSF image cut in CSAS mode for target at
a) (0,0), b) (5mm, 5mm)

Acknowledgment

This work is sponsored by China Scholarship Council (CSC) scholarship program for Joint-training doctorate study in City University of Applied Sciences, Bremen.

Literature

- [1] Dines K.A., Goss S.A.: Computed ultrasonic reflection tomography. *IEEE Transactions on Ultrasonics Ferroelectrics and Frequency Control*, 1987, 34: 309-318.
- [2] Goncharsky A.V., Romanov S.Y., Seryozhnikov S.Y.: A computer simulation study of soft tissue characterization using low-frequency ultrasonic tomography. *Ultrasonics*, 2016, 67: 136-150.
- [3] Choi H., Popovics J.S.: NDE application of ultrasonic tomography to a full-scale concrete structure. *IEEE transactions on ultrasonics, ferroelectrics, and frequency control*, 2015, 62(6): 1076-1085.
- [4] Hayes M.P., Gough P.T.: Synthetic aperture sonar: a review of current status. *IEEE Journal of Oceanic Engineering*, 2009, 34(3): 207-224.
- [5] Denny A.R. et al.: The use of synthetic aperture sonar to survey seafloor massive sulfide deposits. 2015.
- [6] Scheer J., Holm W.A.: Principles of modern radar. SciTech Pub., 2010.